

# Quasiparticle electronic structure of phthalocyanine:TMD interfaces from first-principles *GW*

Olugbenga Adeniran and Zhen-Fei Liu<sup>a)</sup>

Department of Chemistry, Wayne State University, Detroit, Michigan 48202 USA

(Dated: 5 November 2021)

Interfaces formed between monolayer transition metal dichalcogenides (TMDs) and (metallo)phthalocyanine molecules are promising in energy applications and provide a platform for studying mixed-dimensional molecule-semiconductor heterostructures in general. An accurate characterization of the frontier energy level alignment at these interfaces is key in the fundamental understanding of the charge transfer dynamics between the two photon absorbers. Here, we employ the first-principles substrate screening *GW* approach to quantitatively characterize the quasiparticle electronic structure of a series of interfaces: metal-free phthalocyanine ( $H_2Pc$ ) adsorbed on monolayer  $MX_2$  ( $M=Mo, W; X=S, Se$ ) and zinc phthalocyanine ( $ZnPc$ ) adsorbed on  $MoX_2$  ( $X=S, Se$ ). Furthermore, we reveal the dielectric screening effect of the commonly used  $\alpha$ -quartz ( $SiO_2$ ) substrate on the  $H_2Pc:MoS_2$  interface, using the dielectric embedding *GW* approach. Our calculations furnish a systematic set of *GW* results for these interfaces, providing structure-property relationship across a series of similar systems and benchmarks for future experimental and theoretical studies.

## I. INTRODUCTION

Interfaces formed between a pair of semiconductors feature intriguing electronic and optoelectronic properties due to the alignment of the energy levels of one component with respect to the other at the interface. The direction of the charge transfer in the exciton splitting process depends on the type of the heterojunction<sup>1</sup>, which in turn depends on the electronic structure of the interface. Mixed-dimensional heterostructures formed between 0D molecules and 2D substrates<sup>2,3</sup>, in particular organic molecules deposited on monolayer transition metal dichalcogenides (TMDs)<sup>4–6</sup>, have attracted much attention in recent years due to their promising applications in optoelectronic devices<sup>7</sup>, photovoltaics<sup>8</sup>, and photocatalysis<sup>9</sup>. Among all molecular adsorbates, (metallo)phthalocyanines are notably interesting<sup>10,11</sup> by virtue of their structural planarity, large  $\pi$ -conjugation, photon-absorbing capability<sup>12</sup>, fruitful surface chemistry<sup>13</sup>, as well as great tunability in electronic and optical properties via a change of the metal center<sup>14–16</sup>. Once the two photon-absorbers - a (metallo)phthalocyanine molecule and a monolayer TMD - are placed together to form an interface, the underlying electronic structure, i.e., the relative alignment of energy levels of the two components dictates the mechanism and direction of the charge transfer across the interface, giving rise to distinct optoelectronic properties. To quantitatively characterize the electronic structure at these interfaces, various experimental efforts have been put forward<sup>3,17–20</sup>, while benchmark results and a systematic account of the trends are still missing, which constitute the main goals of this paper.

Complementary to experimental techniques, first-principles calculations play a unique role in elucidat-

ing the electronic structure and structure-property relationship, via modelling of atomistically well-defined systems. Notably, the energy levels at a heterogeneous interface pertinent to charge transfer are quasiparticle levels, whose accurate characterization in principle requires methods beyond the conventional density functional theory (DFT). Although many-body perturbation theory (MBPT), such as the *GW* formalism<sup>21–23</sup>, has been very successful<sup>24–26</sup> in resolving the gap problem of DFT<sup>27,28</sup>, its relatively high computational cost hinders its routine applications in large systems such as the interfaces formed between (metallo)phthalocyanines and monolayer TMDs. As a result, most prior computational studies of the phthalocyanine:TMD interfaces still employ DFT, with different complexities such as semi-local functionals<sup>17,29</sup>, hybrid functionals<sup>3,30</sup> or the DFT+*U* approach<sup>31</sup>.

The key ingredient in *GW* that is responsible for an accurate determination of interfacial energy level alignment is the so-called surface polarization<sup>32,33</sup>, or equivalently, dielectric screening due to the substrate. To effectively capture the dielectric screening while reducing the computational cost, the substrate screening *GW* was proposed in Ref. 34, which was shown to be accurate for weakly coupled interfaces with negligible orbital hybridization<sup>34–38</sup>. In this work, we apply this approach to a series of interfaces: metal-free phthalocyanine ( $H_2Pc$ ) adsorbed on monolayer  $MX_2$  ( $M=Mo, W; X=S, Se$ ) and zinc phthalocyanine ( $ZnPc$ ) adsorbed on  $MoX_2$  ( $X=S, Se$ ). We focus on the quasiparticle electronic structure, especially the frontier energy level alignment between the valence band maximum (VBM) and the conduction band minimum (CBM) of the monolayer TMD with the highest occupied molecular orbital (HOMO) and lowest unoccupied molecular orbital (LUMO) of the  $H_2Pc$  or  $ZnPc$ . Our results reveal structure-property relationship and provide *GW*-quality benchmark results for future studies.

Furthermore, in most experimental studies, a sub-

<sup>a)</sup>Electronic mail: zfliu@wayne.edu

strate is used to support the composite molecule:TMD interface system from the bottom, with a commonly used one being  $\alpha$ -quartz ( $\text{SiO}_2$ )<sup>7,20,39-41</sup>. Due to the dielectric screening effect, substrates could greatly affect the electronic properties of the adsorbate on top of it<sup>42-45</sup>. In this work, we use the dielectric embedding  $GW$  approach<sup>46</sup> to address the dielectric effect of the  $\text{SiO}_2$  substrate on the  $\text{H}_2\text{Pc:MoS}_2$  interface. We show that with additional screening from the  $\text{SiO}_2$  underneath, the energy level alignment at the  $\text{H}_2\text{Pc:TMD}$  interface is modulated considerably. Our results on the embedded  $\text{H}_2\text{Pc:MoS}_2$  system agree quantitatively with experimental measurements<sup>41</sup>.

This paper is organized as follows. In Sec. II, we detail the computational methodology and parameters. In Sec. III, we present our results in two aspects: the structure-property relationship across a series of systems and the dielectric effect of the  $\text{SiO}_2$  substrate on the  $\text{H}_2\text{Pc:MoS}_2$  interface. We then conclude in Sec. IV with brief remarks. The Appendix is devoted to draw a quantitative connection between two  $GW$ -based methods that we use, interface  $GW$  and projection  $GW$ , to supplement our discussion in Sec. III B.

## II. METHODOLOGY

As a first step, we relax the in-plane lattice parameter and atomic coordinates of each monolayer TMD unit cell, using the vdw-DF-cx functional<sup>47</sup>. This is the functional that we will use to relax the structure of the interfaces, so we also employ it here to ensure consistency. The calculation uses a  $\mathbf{k}$ -mesh of  $18 \times 18 \times 1$  and a kinetic energy cutoff of 100 Ry. All DFT relaxations employ the optimized norm-conserving Vanderbilt (ONCV) pseudopotentials<sup>48,49</sup> and the Quantum ESPRESSO package<sup>50</sup>. The resulting lattice constants are 3.15 Å, 3.29 Å, 3.15 Å, and 3.28 Å for monolayer  $\text{MoS}_2$ ,  $\text{MoSe}_2$ ,  $\text{WS}_2$ , and  $\text{WSe}_2$ , respectively. These results agree very well with experimental measurements, which yield 3.15 Å<sup>51</sup>, 3.30 Å<sup>52</sup>, 3.15 Å<sup>53</sup>, and 3.28 Å<sup>53</sup> for the four systems, respectively.

After the monolayer unit cell relaxation, we build  $6 \times 6$  supercells and place one  $\text{H}_2\text{Pc}$  molecule flat on each substrate and one  $\text{ZnPc}$  molecule flat on the  $\text{MoS}_2$  and  $\text{MoSe}_2$  substrates to form six interface systems. Each interface simulation cell is 30.0 Å along the  $c$  direction and includes about 23 Å of vacuum. During the relaxation of the interface, the atoms belonging to the substrate are kept fixed in their relaxed monolayer positions, to ensure the exactness of the subsequent reciprocal-space folding of the non-interacting polarizability. The coordinates of the atoms belonging to the adsorbate molecule are full relaxed until all residual forces are below 0.05 eV/Å. The relaxations are carried out using the vdw-DF-cx functional<sup>47</sup>, a  $\mathbf{k}$ -mesh of  $3 \times 3 \times 1$ , and a kinetic energy cutoff of 70 Ry. We found an adsorption height of about 3.0 Å for each system we study, similar to the result of a

prior calculation<sup>3</sup> (3.3 Å). In our relaxed structures, the center of the  $\text{H}_2\text{Pc}$  or  $\text{ZnPc}$  molecule is approximately at the bridge position of two S or Se atoms belonging to the top layer of TMD, which is a stable binding site for similar systems<sup>31</sup>. We note that Ref. 54 reported that the binding energies and band alignments are roughly the same for different binding sites. Fig. 1 shows the relaxed  $\text{H}_2\text{Pc:MoS}_2$  structure in two different views.

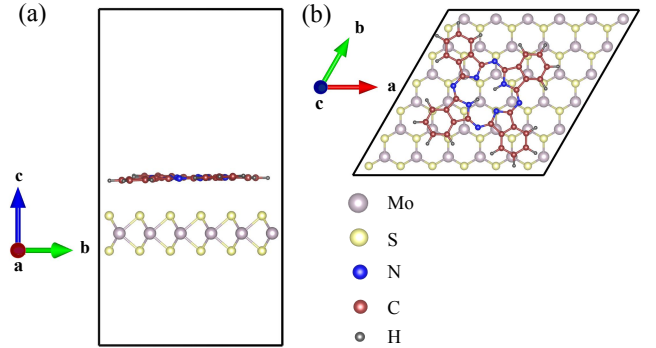


FIG. 1. (a) A side view and (b) a top view of the optimized  $\text{H}_2\text{Pc:MoS}_2$  structure. The black boxes represent periodic boundary conditions. This figure is rendered using VESTA<sup>55</sup>.

Considering the large size of the interfaces and the associated computational cost of conventional  $GW$ , we apply the substrate screening  $GW$  approach<sup>34</sup> for all systems, and have explicitly benchmarked this approach against direct  $GW$  calculations of the  $\text{H}_2\text{Pc:MoS}_2$  and  $\text{H}_2\text{Pc:MoSe}_2$  systems. All  $GW$  calculations are performed at the  $G_0W_0$  level and employ a mean-field starting point using the Perdew-Burke-Ernzerhof (PBE) functional<sup>56</sup>, the Hybertsen-Louie generalized plasmon-pole model<sup>23</sup> for the frequency dependence of the dielectric function, the semiconductor screening for the treatment of the  $\mathbf{q} \rightarrow 0$  limit, the slab Coulomb truncation<sup>57</sup> for the removal of spurious long-range interactions along the  $c$  direction, and the static remainder<sup>58</sup> in the self-energy calculation to improve convergence, as implemented in the BerkeleyGW package<sup>59</sup>. We note that our calculations do not include the spin-orbit coupling, which is known to cause a 0.4-0.5 eV splitting for  $\text{WS}_2$  and  $\text{WSe}_2$  and a 0.1-0.2 eV splitting for  $\text{MoS}_2$  and  $\text{MoSe}_2$  in the valence band<sup>54,60</sup>.

Here we list the computational parameters involved in the substrate screening  $GW$  calculations. For the calculation of the non-interacting polarizability of the substrate unit cell,  $\chi_{\text{sub}}^0$ , we use a  $\mathbf{q}$ -mesh of  $18 \times 18 \times 1$ , a 5 Ry dielectric cutoff, and 200 bands in the summation. For the treatment of the  $\mathbf{q} \rightarrow 0$  limit, 30 bands on a shifted  $\mathbf{q}$ -grid are used. For the calculation of the non-interacting polarizability of the adsorbate molecule,  $\chi_{\text{mol}}^0$ , we use a simulation cell that is the same size along  $a$  and  $b$  as the interface but is much smaller in size (10 Å) along  $c$ . We use a  $\mathbf{q}$ -mesh of  $3 \times 3 \times 1$ , a 5 Ry dielectric cutoff, and 2400 bands in the summation. For the treatment of the  $\mathbf{q} \rightarrow 0$  limit, 360 bands on a shifted  $\mathbf{q}$ -grid are used. After that,

the  $\chi_{\text{sub}}^0$  is folded in the reciprocal space to a  $6 \times 6$  supercell and the  $\chi_{\text{mol}}^0$  is mapped in the real space to the interface simulation cell, following Ref. 34. These quantities are then combined at each  $\mathbf{q}$ -point to approximate  $\chi_{\text{tot}}^0$ , the non-interacting polarizability of the interface. It is then inverted to generate the dielectric function in the interface simulation cell, after which the self-energies are computed (for the details of different approaches employed in this work, see below), where we use a  $\mathbf{k}$ -mesh of  $3 \times 3 \times 1$ , a 5 Ry dielectric cutoff, and 7200 bands of the interface in the summation for the Green's function.

We consider two types of self-energy calculations for each interface, in line with our prior works. (i) “Interface  $GW$ ” calculations, where we compute the expectation value of the self-energy operator using  $\phi^{\text{tot}}$ , an orbital of the interface, i.e.,  $\langle \phi^{\text{tot}} | \Sigma | \phi^{\text{tot}} \rangle$ . (ii) “Projection  $GW$ ” calculations as proposed in Refs. 61,62, where we compute the expectation value of the self-energy operator using an orbital of the freestanding substrate ( $\phi^{\text{sub}}$ ) or that of the freestanding monolayer of adsorbate ( $\phi^{\text{mol}}$ ), i.e.,  $\langle \phi^{\text{sub}} | \Sigma | \phi^{\text{sub}} \rangle$  for the former and  $\langle \phi^{\text{mol}} | \Sigma | \phi^{\text{mol}} \rangle$  for the latter. In both approaches above, the self-energy operator  $\Sigma$  is calculated using  $iG^{\text{tot}}W^{\text{tot}}$ , i.e., both  $G$  and  $W$  are from the interface system with  $W$  calculated using the substrate screening approximation. We compare the interface  $GW$  and projection  $GW$  results for every system, and show that they agree very well except for the LUMO of  $\text{H}_2\text{Pc}$  when  $\text{H}_2\text{Pc}$  is adsorbed on a  $\text{MoS}_2$  substrate. In the Appendix, We show that this discrepancy is due to the strong orbital hybridization and explicitly establish a quantitative connection between the two.

At the end of this section, we clarify the terminologies we use in this paper. All results reported in Sec. III B are obtained using the “substrate screening  $GW$ ”<sup>34</sup> approach, where we compute the self-energy operator using  $iG^{\text{tot}}W^{\text{tot}}$ , together with the approximation  $\chi_{\text{tot}}^0 \approx \chi_{\text{mol}}^0 + \chi_{\text{sub}}^0$ . Within this framework, two types of self-energies are computed: “interface  $GW$ ” -  $\langle \phi^{\text{tot}} | \Sigma | \phi^{\text{tot}} \rangle$ , and “projection  $GW$ ” -  $\langle \phi^{\text{mol}} | \Sigma | \phi^{\text{mol}} \rangle$  or  $\langle \phi^{\text{sub}} | \Sigma | \phi^{\text{sub}} \rangle$ , as discussed above. Note that the “substrate screening  $GW$ ”<sup>34</sup> is physically identical to the “XAF-GW” approach<sup>36</sup>, while the difference between the two is only technical: the former first computes the  $\chi_{\text{mol}}^0$  in a small cell and then performs a real-space mapping of this quantity to the interface simulation cell, hence is more computationally efficient than the latter.

All results reported in Sec. III C are obtained using the “dielectric embedding  $GW$ ” approach<sup>46</sup> (but without the real-space truncation of  $\chi_{\text{sub}}^0$  as done in Ref. 46). Here, we compute  $\langle \phi^{\text{ad}} | \Sigma | \phi^{\text{ad}} \rangle$ , where  $\Sigma = iG^{\text{ad}}W^{\text{tot}}$ . One can see that the key difference here is the use of Green's function of the adsorbate,  $G^{\text{ad}}$ , in the self-energy operator, compared to the “projection  $GW$ ” in the substrate screening framework. Because of this difference, the “dielectric embedding  $GW$ ” further reduces the computational cost without sacrificing the accuracy, for weakly coupled interfaces. Note that in Sec. III C, the “adsorbate” itself is already a  $\text{H}_2\text{Pc}:\text{MoS}_2$  interface (such that

both  $G^{\text{ad}}$  and  $\phi^{\text{ad}}$  are for the  $\text{H}_2\text{Pc}:\text{MoS}_2$ ) and only the  $\text{SiO}_2$  substrate is included implicitly as a dielectric environment through  $W^{\text{tot}}$ , such that the “weak coupling” condition is satisfied.

### III. RESULTS AND DISCUSSION

#### A. Convergence Study

$GW$  calculations are known to converge slowly. We describe our convergence study in this section to show that our calculations are reasonably well converged and the level alignment results are reliable.

For the monolayer  $\text{MoS}_2$  unit cell, we have checked that compared to a 10 Ry dielectric cutoff and 1000 bands in the summation, our choice of parameters (5 Ry and 200 bands) lead to a convergence in the band gap within 0.02 eV, although the individual quasiparticle energies are off by about 0.3 eV. Our prediction of the monolayer  $\text{MoS}_2$  gap is 2.81 eV, in good agreement with prior  $GW$  calculations<sup>63</sup> (2.80 eV). We also note that for such low-dimensional materials, the nonuniform neck subsampling method<sup>64</sup> (NNS) leads to faster convergence. Although we do not use it here for the interface, our calculations of the monolayer  $\text{MoS}_2$  unit cell achieve reasonably good agreement (within 0.1 eV in the gap) with NNS results with a 10 Ry dielectric cutoff.

For the interface systems, using  $\text{H}_2\text{Pc}:\text{MoSe}_2$  as an example, we have checked that our choice of parameters (a 5 Ry dielectric cutoff and 7200 bands) lead to a convergence of the quasiparticle energies and energy level alignments at the interface within 0.05 eV, compared to using a 7.5 Ry cutoff and 9000 bands in the summation. This choice of parameter is thus adopted for all other interface systems.

#### B. Molecule:TMD Interfaces

When a molecule is adsorbed on a semiconductor substrate, the interface could in principle exhibit the so-called type-I (straddling band gap), type-II (staggered band gap), or type-III (broken band gap) energy level alignment<sup>1</sup>. Specific to the  $\text{H}_2\text{Pc}:\text{TMD}$  or  $\text{ZnPc}:\text{TMD}$  interfaces studied in this work, type-I and type-II heterostructures are possible, based on our results below. Depending on the relative ordering between TMD and molecular levels, we further categorize the interfaces to type-Ia, type-Ib, type-IIa, and type-IIb, as schematically shown in Fig. 2(a)-(d), respectively. All interfaces studied in this work have direct band gap at  $\Gamma$ , so all interface gaps and energy level alignments are reported for the  $\Gamma$  point.

In Fig. 2, we show frontier energy levels (bands) of the freestanding monolayer TMD and those of the freestanding molecular layer, together with their counterparts within the interface. Blue lines represent TMD

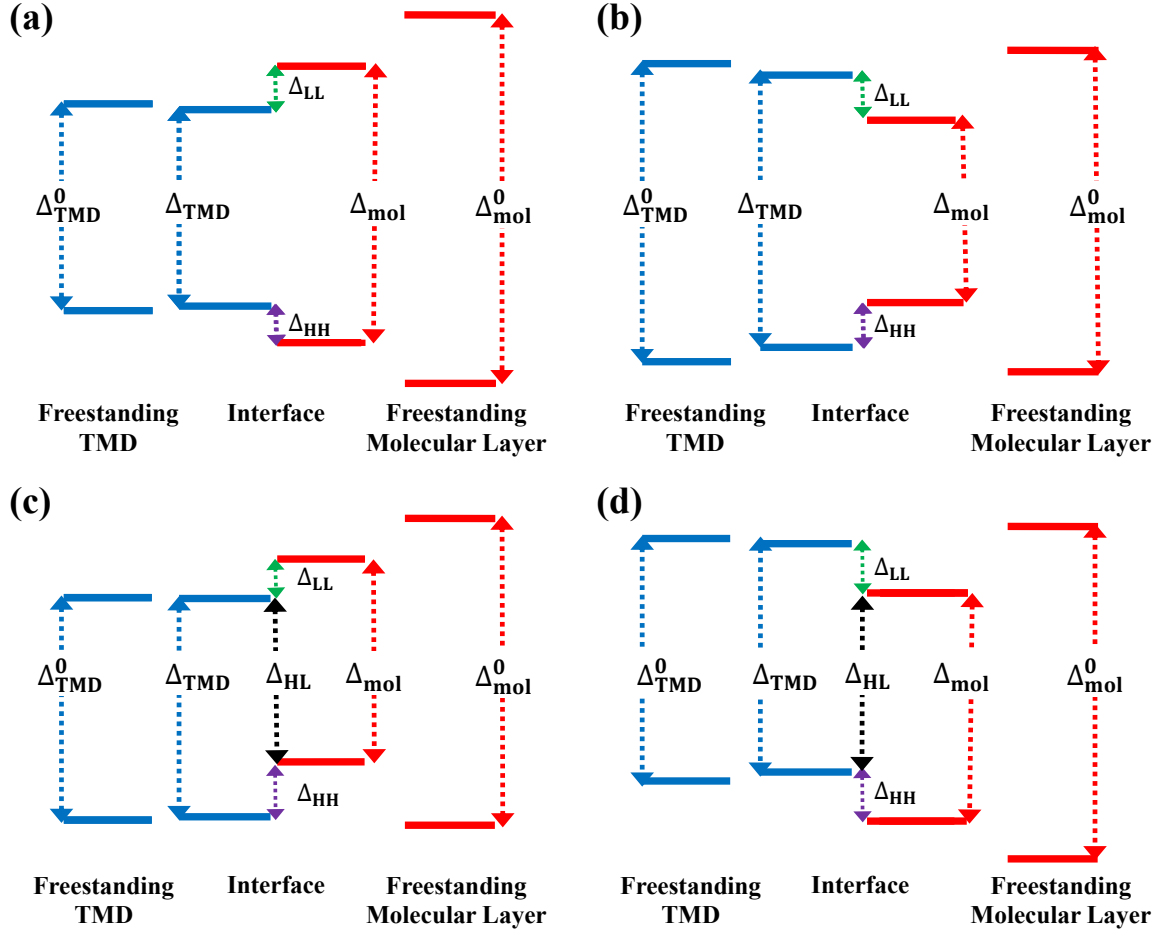


FIG. 2. Energy level alignment diagrams showing relevant gaps across the interface.  $\Delta_{\text{TMD}}^0$  ( $\Delta_{\text{mol}}^0$ ) is the band gap of the TMD monolayer ( $\text{H}_2\text{Pc}$  or  $\text{ZnPc}$  molecular layer) in its freestanding form, while  $\Delta_{\text{TMD}}$  ( $\Delta_{\text{mol}}$ ) is the gap of the TMD ( $\text{H}_2\text{Pc}$  or  $\text{ZnPc}$ ) within the interface system.  $\Delta_{\text{LL}}$  ( $\Delta_{\text{HH}}$ ) is the gap between the TMD CBM (VBM) and the LUMO (HOMO) of the molecular layer. (a) and (b) display type-I heterostructures between TMD and the molecule. In (a) [(b)], both the VBM and CBM of the interface are localized on the TMD (molecule), which we denote “type-Ia” (“type-Ib”). (c) and (d) display type-II heterostructures between TMD and the molecule. In (c) [(d)], the VBM of the interface is localized on the molecule (TMD) and the CBM of the interface is localized on the TMD (molecule), which we denote “type-IIa” (“type-IIb”). In both (c) and (d),  $\Delta_{\text{HL}}$  denotes the band gap of the interface.

TABLE I. Key descriptors of the electronic structure for different interface systems as calculated from DFT (using the PBE functional) and  $GW$ . All values are in eV.  $\Delta_{\text{TMD}}^0$  and  $\Delta_{\text{mol}}^0$  are the band gaps of the freestanding TMD monolayer and molecular layer, respectively.  $\Delta_{\text{TMD}}^0$  is calculated at the  $K$  point for the unit cell, and  $\Delta_{\text{mol}}^0$  is calculated at the  $\Gamma$  point.  $\Delta_{\text{TMD}}$ ,  $\Delta_{\text{LL}}$ ,  $\Delta_{\text{HL}}$ ,  $\Delta_{\text{HH}}$ , and  $\Delta_{\text{mol}}$  are energy level differences within the interface systems defined in Fig. 2, all calculated at the  $\Gamma$  point.

Interface	Method	Type	$\Delta_{\text{TMD}}^0$	$\Delta_{\text{TMD}}$	$\Delta_{\text{LL}}$	$\Delta_{\text{HL}}$	$\Delta_{\text{HH}}$	$\Delta_{\text{mol}}$	$\Delta_{\text{mol}}^0$
$\text{H}_2\text{Pc}:\text{MoS}_2$	DFT	Ia, Fig. 2(c)	1.79	1.79	0.09	1.21	0.58	1.30	1.39
	$GW$	Ia, Fig. 2(c)	2.81	2.78	0.14	2.33	0.45	2.47	3.86
$\text{H}_2\text{Pc}:\text{MoS}_2:\text{SiO}_2$	$GW$	Ia, Fig. 2(c)	2.81	2.07	0.68	1.62	0.45	2.30	3.86
	DFT	IIb, Fig. 2(d)	1.55	1.55	0.24	1.31	0.06	1.37	1.37
$\text{H}_2\text{Pc}:\text{MoSe}_2$	$GW$	Ia, Fig. 2(a)	2.40	2.39	0.20	—	0.18	2.77	3.86
	DFT	Ib, Fig. 2(b)	1.93	1.96	0.24	—	0.36	1.36	1.36
$\text{H}_2\text{Pc}:\text{WS}_2$	$GW$	Ia, Fig. 2(c)	3.05	2.98	0.14	2.76	0.22	2.90	3.86
	DFT	IIb, Fig. 2(d)	1.68	1.65	0.54	1.11	0.26	1.37	1.39
$\text{H}_2\text{Pc}:\text{WSe}_2$	$GW$	Ia, Fig. 2(a)	2.65	2.44	0.05	—	0.35	2.84	3.86
	DFT	IIa, Fig. 2(c)	1.79	1.80	0.27	1.15	0.65	1.42	1.42
$\text{ZnPc}:\text{MoS}_2$	DFT	Ia, Fig. 2(c)	2.81	2.78	0.59	2.29	0.49	2.88	3.91
	$GW$	Ia, Fig. 2(b)	1.55	1.55	0.16	—	0.04	1.35	1.35
$\text{ZnPc}:\text{MoSe}_2$	DFT	Ib, Fig. 2(b)	2.40	2.38	0.28	—	0.30	2.96	3.91
	$GW$	Ia, Fig. 2(a)	—	—	—	—	—	—	—

levels and red lines represent molecular levels. We discuss the following quantities that characterize the electronic structure of these interfaces:  $\Delta_{\text{TMD}}^0$  ( $\Delta_{\text{mol}}^0$ ) is the band gap of the TMD monolayer ( $\text{H}_2\text{Pc}$  or  $\text{ZnPc}$  molecular layer) in its freestanding form, while  $\Delta_{\text{TMD}}$  ( $\Delta_{\text{mol}}$ ) is the gap of the TMD ( $\text{H}_2\text{Pc}$  or  $\text{ZnPc}$ ) within the interface system.  $\Delta_{\text{LL}}$  ( $\Delta_{\text{HH}}$ ) is the gap between the TMD CBM (VBM) and the LUMO (HOMO) of the molecular layer, which is of interest for both type-I and type-II heterostructures, because the sign and magnitude of  $\Delta_{\text{LL}}$  ( $\Delta_{\text{HH}}$ ) dictate the direction and barrier for electron (hole) transfer across the interface, respectively. For the type-II heterostructures in Fig. 2(c)(d), we further consider  $\Delta_{\text{HL}}$ , the fundamental (transport) gap of the entire interface, which is between the HOMO of the molecule (the VBM of the TMD) and the CBM of the TMD (the LUMO of the molecule) for type-IIa (type-IIb).  $\Delta_{\text{TMD}}^0$  is calculated at the  $K$  point of the Brillouin zone for the TMD unit cell, and all other quantities are calculated at the  $\Gamma$  point.

Table I shows the computed results for all quantities labelled in Fig. 2, from both DFT and substrate screening  $GW$ . To verify that the substrate screening approximation holds for the systems, we compare substrate screening  $GW$  results with direct  $GW$  calculations for two interfaces,  $\text{H}_2\text{Pc}:\text{MoS}_2$  and  $\text{H}_2\text{Pc}:\text{MoSe}_2$ . This comparison shows that the substrate screening  $GW$  is very accurate: for all quantities reported in Table I, substrate screening  $GW$  leads to an agreement with direct  $GW$  results within 0.05 eV. With the same accuracy, the substrate screening  $GW$  approach costs only about 30% in computing time and 10% in memory (for the  $\chi$  step) compared to the direct  $GW$  for the systems studied. We also note that our  $GW$  results on  $\text{H}_2\text{Pc}:\text{MoS}_2$  and  $\text{ZnPc}:\text{MoS}_2$  are largely in agreement with other calculations of the same systems (but with slightly different simulation cells) using range-separated hybrid functionals<sup>65</sup> and  $GW^{54}$ .

Figure 3 shows the  $GW$  interfacial energy level alignment for the six heterostructures, where we use different colors to represent different substrates or molecules and all energy levels are measured with respect to a common vacuum. In Figure 3, solid bars or lines are interface  $GW$  results (same as those reported in Table I), i.e.,  $\langle \phi^{\text{tot}} | \Sigma[G^{\text{tot}} W^{\text{tot}}] | \phi^{\text{tot}} \rangle$ , where the  $\phi^{\text{tot}}$  is chosen as the interface orbital that mostly resembles the orbital of interest (HOMO, LUMO, VBM, or CBM) of the freestanding monolayer TMD or molecular layer, as quantitatively determined from orbital projections. Dashed lines are projection  $GW$  results, i.e.,  $\langle \phi^{\text{sub}} | \Sigma[G^{\text{tot}} W^{\text{tot}}] | \phi^{\text{sub}} \rangle$  for the TMD, where  $\phi^{\text{sub}}$  is the VBM or CBM of the freestanding TMD, and  $\langle \phi^{\text{mol}} | \Sigma[G^{\text{tot}} W^{\text{tot}}] | \phi^{\text{mol}} \rangle$  for the molecule, where  $\phi^{\text{mol}}$  is the HOMO or LUMO of the freestanding molecular layer. For all cases except the  $\text{H}_2\text{Pc}$  LUMO on  $\text{MoS}_2$  substrate, the interface  $GW$  results agree very well with projection  $GW$  results, which indicates negligible orbital hybridization upon formation of the interface, such that  $\langle \phi^{\text{tot}} | \phi^{\text{sub}} \rangle$  and  $\langle \phi^{\text{tot}} | \phi^{\text{mol}} \rangle$  are close to unity. The special case of  $\text{H}_2\text{Pc}$  LUMO on  $\text{MoS}_2$

substrate is discussed in the Appendix.

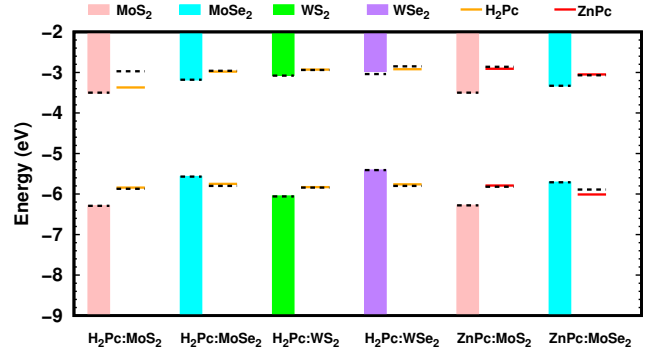


FIG. 3. Energy level alignment for the molecule:TMD interfaces as calculated from substrate screening  $GW$ . The bars denote the bands of  $\text{MoS}_2$  (pink),  $\text{MoSe}_2$  (blue),  $\text{WS}_2$  (green), and  $\text{WSe}_2$  (purple). The lines denote the energy levels of  $\text{H}_2\text{Pc}$  (orange) and  $\text{ZnPc}$  (red). Solid bars or lines indicate results from interface  $GW$  calculations (same as those in Table I) and dashed lines indicate results from projection  $GW$  calculations. All energy levels are measured with respect to vacuum.

Below in this section, we discuss the results from three aspects: (i) the renormalization of gaps upon the formation of the interface; (ii) the qualitative difference between DFT and  $GW$  in the prediction of the type of some heterostructures; and (iii) the structure-property relationship across the six different systems.

For the freestanding monolayer TMD, our  $GW$  calculations yield band gaps of 2.81 eV, 2.40 eV, 3.05 eV, and 2.65 eV for  $\text{MoS}_2$ ,  $\text{MoSe}_2$ ,  $\text{WS}_2$ , and  $\text{WSe}_2$ , respectively. Our results are in good agreement with Ref. 63, where  $\text{sc}GW_0$  calculations of monolayer TMDs with similar lattice parameters (within 0.01 Å of our relaxed values) were performed, resulting in band gaps of 2.80 eV, 2.40 eV, 3.11 eV, and 2.68 eV, respectively, for the four materials. For the freestanding  $\text{H}_2\text{Pc}$  ( $\text{ZnPc}$ ) molecular layer, our  $GW$  calculations yield a HOMO-LUMO gap of 3.86 eV (3.91 eV) and an ionization potential of 6.24 eV (6.16 eV), on par with Ref. 66, where  $GW$  calculation of an isolated  $\text{H}_2\text{Pc}$  molecule yielded a band gap of 3.67 eV and an ionization potential of 6.08 eV. The difference between our results and Ref. 66 lies in the physical difference between a periodic molecular layer and an isolated molecule.

At the interface, the gap renormalization for the  $\text{H}_2\text{Pc}$  or  $\text{ZnPc}$  molecule is significant, with about 1 eV decrease in the HOMO-LUMO gap when the molecule is brought in contact with the substrate. This is consistent with well-established understanding of the surface renormalization at molecule-substrate interfaces<sup>32,33</sup>. On the contrary, Table I shows that TMD band gaps are still very similar to those of the freestanding phase, indicating negligible gap renormalization for the substrate, which we attribute to the relatively low coverage of the molecule on the substrate (see Fig. 1). This situation is different from a previous semiconductor-semiconductor interface

that we studied before<sup>37</sup>, where we observed gap renormalization on both sides of an organic bulk heterojunction. For the H<sub>2</sub>Pc:MoS<sub>2</sub>:SiO<sub>2</sub> interface, the MoS<sub>2</sub> gap is significantly renormalized due to the dielectric screening effect of the extensive SiO<sub>2</sub> substrate underneath, as we will elaborate in Sec. III C below. Needless to say, DFT clearly underestimates the relevant gaps, and does not capture the gap renormalization at the interface.

A remarkable observation here is that for some systems, DFT and *GW* yield qualitatively different heterostructure type, as listed in Table I. To be specific, for H<sub>2</sub>Pc:MoSe<sub>2</sub> and H<sub>2</sub>Pc:WSe<sub>2</sub>, DFT predicts a type-II while *GW* predicts a type-I interface; for H<sub>2</sub>Pc:WS<sub>2</sub>, DFT predicts a type-I while *GW* predicts a type-II interface; for ZnPc:MoSe<sub>2</sub>, although both DFT and *GW* predict type-I, the relative ordering of TMD and molecular levels are opposite (type-Ia and type-Ib as shown in Fig. 2). In all cases, it is the self-energy correction to the LUMO of the molecular adsorbate that pushes this orbital upward in energy, causing a change in the heterostructure type (there is an additional effect in ZnPc:MoSe<sub>2</sub>, where the self-energy correction to the HOMO of ZnPc shifts this orbital downward). We note that experimental characterizations of these quasiparticle energy level alignments require techniques such as (inverse) photoemission spectroscopy, while most existing experiments<sup>3,7,18,20,67,68</sup> focused on the description of excitons at such interfaces using, e.g., photoluminescence. Although we have not found direct experimental verification of most of the quasiparticle energy level alignments that we have computed (except for H<sub>2</sub>Pc:MoS<sub>2</sub>:SiO<sub>2</sub>), we believe our work provides a reference point for future experiments.

Table I and Fig. 3 reveal structure-property relationship that is helpful in materials design of similar systems. All sulfur-based interfaces form type-IIa heterostructures with HOMO (LUMO) of the adsorbed molecule lying higher than VBM (CBM) of the TMD substrate. All selenium-based ones form type-Ia heterostructures with HOMO (LUMO) of the adsorbed molecule lying lower (higher) than the VBM (CBM) of the TMD substrate. The gap renormalization of H<sub>2</sub>Pc is larger on Mo-based substrates, compared to the W-based counterparts. Moreover, comparing ZnPc with H<sub>2</sub>Pc on the same substrates, we find that the gap renormalization of ZnPc is smaller, resulting in larger  $\Delta_{LL}$  and  $\Delta_{HH}$  values than H<sub>2</sub>Pc-based interfaces. Since these values represent the charge transfer barrier across the interface in the exciton splitting process, this trend suggests that the electron or hole transfer rates across H<sub>2</sub>Pc-based interfaces might be generally higher than those across ZnPc-based interfaces.

### C. The Effect of SiO<sub>2</sub> substrate on the H<sub>2</sub>Pc:MoS<sub>2</sub> Interface

In typical experimental studies, the molecule:TMD interfaces are further supported by a substrate underneath

the monolayer TMD<sup>41,42</sup>. It is well known that the band gaps of TMDs are sensitive to the dielectric environment provided by other adjacent 2D materials or substrates<sup>43,44,69</sup>. Therefore, it is imperative to include the dielectric screening effects from any additional substrates to achieve quantitative agreement with experimental characterization of the electronic structure of the molecule:TMD interfaces. In this work, we employ the dielectric embedding *GW* approach as developed in Ref. 46 to include the effect of the substrate, using the H<sub>2</sub>Pc:MoS<sub>2</sub> system as an example. We focus on this system because an experimental measurement is available<sup>41</sup> for a direct comparison.

A commonly used substrate in experimental studies of molecule:TMD interfaces is the  $\alpha$ -quartz (SiO<sub>2</sub>)<sup>3,7,20,39-41</sup>. To model the composite H<sub>2</sub>Pc:MoS<sub>2</sub>:SiO<sub>2</sub> system, we have applied a 5% compressive strain to the experimental lattice constant of SiO<sub>2</sub> to enforce a commensurate simulation cell with H<sub>2</sub>Pc:MoS<sub>2</sub>. Under this strain, the PBE band gap of 5.93 eV for bulk SiO<sub>2</sub><sup>70</sup> increases by about 4% while other qualitative features of the band structure remain intact. Using the dielectric embedding *GW* approach<sup>46</sup>, we first compute the non-interacting polarizability of the SiO<sub>2</sub> substrate in its unit cell, then fold this quantity in reciprocal space to the supercell, and lastly, combine the folded quantity with the non-interacting polarizability of the H<sub>2</sub>Pc:MoS<sub>2</sub> (which in turn is calculated using the substrate screening *GW*<sup>34</sup> approach). As a result, the self-energy calculation is only explicitly performed for the H<sub>2</sub>Pc:MoS<sub>2</sub> interface, where the *W* includes the dielectric effect of the SiO<sub>2</sub> substrate.

The dielectric embedding *GW* approach<sup>46</sup> applied here adds little extra computational cost compared to the *GW* calculation of H<sub>2</sub>Pc:MoS<sub>2</sub> without the SiO<sub>2</sub> substrate. The inner products between the H<sub>2</sub>Pc:MoS<sub>2</sub> orbitals of interest (the orbitals that represent the resonances of H<sub>2</sub>Pc HOMO/LUMO and MoS<sub>2</sub> VBM/CBM) and the H<sub>2</sub>Pc:MoS<sub>2</sub>:SiO<sub>2</sub> orbitals are close to unity, suggesting negligible orbital hybridization between H<sub>2</sub>Pc:MoS<sub>2</sub> and SiO<sub>2</sub> and the validity of the dielectric embedding *GW* approach. We note in passing that within this approach, the orbital hybridization *within* H<sub>2</sub>Pc:MoS<sub>2</sub>, i.e., between H<sub>2</sub>Pc and MoS<sub>2</sub>, is captured exactly.

Fig. 4(a) shows the optimized structure of the H<sub>2</sub>Pc:MoS<sub>2</sub>:SiO<sub>2</sub> system, where we consider a two-layer SiO<sub>2</sub> substrate with silicon termination. Other terminations exist<sup>71,72</sup>, and we have checked explicitly that for a hydrogen-passivated SiO<sub>2</sub> surface, the band alignment results stay unchanged compared to what we will report below. The separation between the SiO<sub>2</sub> and MoS<sub>2</sub> is optimized using vdw-DF-cx to be 3.5 Å. Fig. 4(b) shows the quasiparticle electronic structure of the H<sub>2</sub>Pc:MoS<sub>2</sub> interface embedded in the dielectric environment of SiO<sub>2</sub>, computed using the dielectric embedding *GW* approach<sup>46</sup>, with key energy gaps listed in Table I. Compared to the H<sub>2</sub>Pc:MoS<sub>2</sub> system without the SiO<sub>2</sub> substrate, the MoS<sub>2</sub> band gap is further renormalized to

2.07 eV due to the additional dielectric screening from  $\text{SiO}_2$ , which is in very good agreement with experiment (2.10 eV as in Ref. 41). The  $\text{H}_2\text{Pc}$  gap is further renormalized only moderately, possibly due to its large distance to the  $\text{SiO}_2$  substrate. Furthermore, the  $\Delta_{\text{LL}}$  is considerably changed to 0.68 eV (compared to 0.14 eV without the  $\text{SiO}_2$  substrate), and the  $\Delta_{\text{HL}}$  is changed to 1.62 eV (compared to 2.33 eV without the  $\text{SiO}_2$  substrate). Interestingly, the  $\Delta_{\text{HH}}$  does not change compared to the case without the  $\text{SiO}_2$  substrate.

As a direct comparison with experiment, Ref. 41 characterized the energy level alignment of the  $\text{H}_2\text{Pc}:\text{MoS}_2$  interface deposited on  $\text{SiO}_2$  substrate. Ultraviolet photoemission spectroscopy and inverse photoemission spectroscopy measurements were performed for pristine monolayer  $\text{MoS}_2$  and the  $\text{H}_2\text{Pc}:\text{MoS}_2$  interface, both on the  $\text{SiO}_2$  substrate. By aligning the Fermi level of the two systems, Ref. 41 deduced that  $\Delta_{\text{TMD}} = 2.1$  eV,  $\Delta_{\text{LL}} = 1.0$  eV,  $\Delta_{\text{HL}} = 1.2$  eV,  $\Delta_{\text{HH}} = 0.9$  eV, and  $\Delta_{\text{mol}} = 2.2$  eV. We note that our results agree quantitatively with Ref. 41 in  $\Delta_{\text{TMD}}$  and  $\Delta_{\text{mol}}$  values, but our computed  $\text{H}_2\text{Pc}$  HOMO and LUMO levels are both lower by 0.3–0.4 eV than those reported in Ref. 41, resulting in lower  $\Delta_{\text{LL}}$ , lower  $\Delta_{\text{HH}}$  and higher  $\Delta_{\text{HL}}$ . We discuss two possible sources for the discrepancy. First, Ref. 41 aligned the Fermi level of the pristine  $\text{MoS}_2$  (without the  $\text{H}_2\text{Pc}$  adsorbate) and that of the  $\text{H}_2\text{Pc}:\text{MoS}_2$  interface. The precise position of the Fermi level within the band gap might depend on the specific experimental condition, while it is not well-defined in first-principles calculations at zero temperature. This difference between an experiment and a computation affects how the  $\text{MoS}_2$  and  $\text{H}_2\text{Pc}$  levels are relatively aligned without affecting the band gap of each component. Second, the coverage of the  $\text{H}_2\text{Pc}$  adsorbate on  $\text{MoS}_2$  substrate might be different between Ref. 41 and our modelling, which might lead to different interface dipoles and consequently different  $\Delta_{\text{LL}}$ ,  $\Delta_{\text{HL}}$ , and  $\Delta_{\text{HH}}$  values.

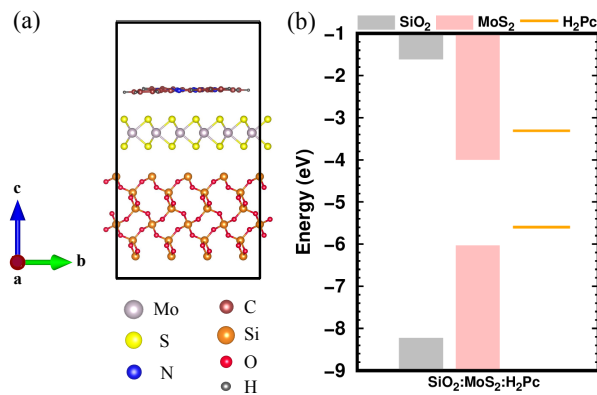


FIG. 4. (a) Optimized structure of the  $\text{H}_2\text{Pc}:\text{MoS}_2:\text{SiO}_2$  interface. (b) Quasiparticle energy level alignment from an embedding  $GW$  calculation, where the  $\text{H}_2\text{Pc}:\text{MoS}_2$  interface is embedded into a dielectric environment of a  $\text{SiO}_2$  substrate. All energy levels are measured with respect to vacuum.

The result is a clear indication of the dielectric screening effect of the substrate on molecule:TMD interfaces. Our dielectric embedding  $GW$  approach provides an accurate account of this effect without further increasing the computational cost, compared to calculations that only involve molecule:TMD interfaces. Lastly, we note in passing that our calculated  $GW$  band gap is 8.69 eV for bulk  $\text{SiO}_2$ , in agreement with Ref. 73, which reports a  $GW$  gap of 8.77 eV. Our  $GW$  gap is 7.10 eV for the free-standing bilayer  $\text{SiO}_2$  with Si termination, and 6.64 eV when the bilayer  $\text{SiO}_2$  is in contact with monolayer  $\text{MoS}_2$ , as shown in Fig. 4(b). These gaps are large enough such that the precise positioning of  $\text{SiO}_2$  band edges relative to TMD bands will unlikely have large effects on the energy level alignment at the  $\text{H}_2\text{Pc}:\text{MoS}_2$  interface.

#### IV. CONCLUSION

In this work, we have systematically and quantitatively characterized the quasiparticle electronic structure of a series of interfaces formed between (metallo)pathalocyanine molecules and monolayer TMDs, using first-principles  $GW$  calculations. Besides the well-known gap renormalization of the adsorbate, we have found that in certain cases,  $GW$  and DFT yield qualitatively different heterostructure types, which is of interest for future experimental validation. Furthermore, we have elucidated the dielectric screening effect of the  $\text{SiO}_2$  substrate on the electronic structure of  $\text{H}_2\text{Pc}:\text{MoS}_2$ , leading to quantitative agreement with existing experiments. Our findings provide useful structure-property relationship for materials design, insight into charge transfer processes across such molecule:TMD interfaces, as well as benchmark data for future theoretical and experimental investigations.

#### ACKNOWLEDGMENTS

Z.-F.L. acknowledges support from an NSF CAREER Award, DMR-2044552. O.A. acknowledges A. Paul and Carole C. Schaap Endowed Distinguished Graduate Award and Rumble Fellowship from Wayne State University. This research used computational resources at Wayne State Grid and additionally via a user project at Center for Nanoscale Materials at Argonne National Laboratory, an Office of Science user facility, which was supported by the U.S. Department of Energy, Office of Science, Office of Basic Energy Sciences, under Contract No. DE-AC02-06CH11357. Furthermore, large-scale calculations used computational resources from the National Energy Research Scientific Computing Center (NERSC), a U.S. Department of Energy Office of Science User Facility operated under Contract No. DE-AC02-05CH11231.

## AUTHOR DECLARATIONS

The authors have no conflicts to disclose.

## DATA AVAILABILITY STATEMENT

The data that support the findings of this study are available from the corresponding author upon reasonable request.

### Appendix A: Deriving projection $GW$ results from interface $GW$ calculations

We investigate the quantitative difference between projection  $GW$  calculations (dashed lines in Fig. 3) and interface  $GW$  calculations (solid lines in Fig. 3). They agree very well except for the H<sub>2</sub>Pc LUMO on MoS<sub>2</sub> substrate, which involves strong orbital hybridization. Here, we quantitatively connect the projection  $GW$  results with interface  $GW$  results.

To make the discussion self-contained in the Appendix, we repeat here that in “projection  $GW$ ”<sup>61,62</sup>, we compute  $\langle \phi^{\text{sub}} | \Sigma | \phi^{\text{sub}} \rangle$  for the TMD substrate and  $\langle \phi^{\text{mol}} | \Sigma | \phi^{\text{mol}} \rangle$  for the adsorbed molecule, where  $\phi^{\text{sub}}$  ( $\phi^{\text{mol}}$ ) is an orbital of the *freestanding* substrate (molecule). In “interface  $GW$ ”, we compute  $\langle \phi^{\text{tot}} | \Sigma | \phi^{\text{tot}} \rangle$  with  $\phi^{\text{tot}}$ , where  $\phi^{\text{tot}}$  is an orbital of the interface that most resembles a substrate or molecular orbital (i.e., a resonance). In both cases,  $\Sigma$  is the same operator that involves the  $G$  and  $W$  of the entire interface.

We focus on the H<sub>2</sub>Pc LUMO on MoS<sub>2</sub> substrate, and expand the H<sub>2</sub>Pc LUMO (calculated for the freestanding H<sub>2</sub>Pc molecular layer in the same simulation cell as the interface) in terms of the orbitals of the H<sub>2</sub>Pc:MoS<sub>2</sub> interface:

$$|\phi_{\text{LUMO}}^{\text{mol}}\rangle = C_1 |\phi_{\text{CBM+2}}^{\text{tot}}\rangle + C_2 |\phi_{\text{CBM+8}}^{\text{tot}}\rangle + C_3 |\phi_{\text{CBM+9}}^{\text{tot}}\rangle. \quad (\text{A1})$$

Here, we have neglected expansion coefficients whose magnitude is below 0.05. The projection  $GW$  computes  $\langle \phi_{\text{LUMO}}^{\text{mol}} | \Sigma | \phi_{\text{LUMO}}^{\text{mol}} \rangle$ . Substituting Eq. (A1), this quantity is related to diagonal and off-diagonal matrix elements of  $\Sigma$  involving the three interface orbitals on the right-hand side of Eq. (A1). These matrix elements are from *interface  $GW$*  calculations, which are then connected to projection  $GW$  results that involve the left-hand side of Eq. (A1). For diagonal elements, we use the difference between the quasiparticle energies and the corresponding Kohn-Sham eigenvalues. For off-diagonal elements, we use the matrix elements of  $\Sigma - V_{\text{xc}}$  with  $V_{\text{xc}}$  being the exchange-correlation operator.

The expansion coefficients and matrix elements (in eV) are:

$$C_1 = 0.6358 - 0.0647i, C_2 = -0.6046 + 0.0615i, C_3 = -0.4379 + 0.0446i;$$

$$\begin{aligned} \langle \phi_{\text{CBM+2}}^{\text{tot}} | \Sigma | \phi_{\text{CBM+2}}^{\text{tot}} \rangle &= 0.667, \langle \phi_{\text{CBM+8}}^{\text{tot}} | \Sigma | \phi_{\text{CBM+8}}^{\text{tot}} \rangle = 0.871, \langle \phi_{\text{CBM+9}}^{\text{tot}} | \Sigma | \phi_{\text{CBM+9}}^{\text{tot}} \rangle = 0.876; \\ \langle \phi_{\text{CBM+2}}^{\text{tot}} | \Sigma | \phi_{\text{CBM+8}}^{\text{tot}} \rangle &= -0.227 + 0.222i, \\ \langle \phi_{\text{CBM+2}}^{\text{tot}} | \Sigma | \phi_{\text{CBM+9}}^{\text{tot}} \rangle &= -0.225 + 0.244i, \\ \langle \phi_{\text{CBM+8}}^{\text{tot}} | \Sigma | \phi_{\text{CBM+9}}^{\text{tot}} \rangle &= -0.104 + 0.001i. \end{aligned}$$

Using these values from an interface  $GW$  calculation, one can calculate from Eq. (A1) that  $\langle \phi_{\text{LUMO}}^{\text{mol}} | \Sigma | \phi_{\text{LUMO}}^{\text{mol}} \rangle = 1.011$  eV. This is in very good agreement with the projection  $GW$  calculation of the H<sub>2</sub>Pc LUMO on MoS<sub>2</sub>, whose self-energy correction is 1.023 eV. The above analysis successfully explains the difference between the solid and dashed lines in Fig. 3: the solid line computes  $\langle \phi_{\text{CBM+2}}^{\text{tot}} | \Sigma | \phi_{\text{CBM+2}}^{\text{tot}} \rangle$ , which only involves the first term on the right-hand side of Eq. (A1), while the dashed line computes  $\langle \phi_{\text{LUMO}}^{\text{mol}} | \Sigma | \phi_{\text{LUMO}}^{\text{mol}} \rangle$ , which involves the left-hand side of Eq. (A1).

As a limiting case, if only one of the coefficients in Eq. (A1) is unity, then the isolated molecular orbital and its resonance at the interface are the same (the weak-coupling limit). The projection  $GW$  and the interface  $GW$  will then yield identical values in the quasiparticle energy. This is, in fact, a very good approximation for most interfaces. Specific to the systems studied in this work, the two approaches agree well for every resonance except for the H<sub>2</sub>Pc LUMO on the MoS<sub>2</sub> substrate.

### Appendix B: Deriving interface $GW$ results from projection $GW$ calculations

In a similar manner to the above analysis, we can derive interface  $GW$  results from projection  $GW$  calculations of the substrate and of the adsorbate, which can also explain the difference between the solid and dashed lines in Fig. 3. For the H<sub>2</sub>Pc LUMO on MoS<sub>2</sub> substrate, its resonance in the interface is the CBM+2 of the interface. We then consider the following expansion:

$$|\phi_{\text{CBM+2}}^{\text{tot}}\rangle = B_1 |\phi_{\text{LUMO}}^{\text{mol}}\rangle + B_2 |\phi_{\text{CBM+6}}^{\text{TMD}}\rangle + B_3 |\phi_{\text{CBM+3}}^{\text{TMD}}\rangle \quad (\text{B1})$$

We again neglect expansion coefficients whose magnitude is below 0.05. The left-hand side of Eq. (B1) is the orbital used in an interface  $GW$  calculation, and the right-hand side consists of orbitals used in projection  $GW$  calculations of the substrate and of the adsorbate, respectively.

The expansion coefficients and the matrix elements (in eV) are:

$$\begin{aligned} B_1 &= 0.6358 + 0.0647i, B_2 = -0.6156 - 0.1232i, B_3 = -0.3509 - 0.0703i; \\ \langle \phi_{\text{LUMO}}^{\text{mol}} | \Sigma | \phi_{\text{LUMO}}^{\text{mol}} \rangle &= 1.023, \langle \phi_{\text{CBM+6}}^{\text{TMD}} | \Sigma | \phi_{\text{CBM+6}}^{\text{TMD}} \rangle = 0.445, \langle \phi_{\text{CBM+3}}^{\text{TMD}} | \Sigma | \phi_{\text{CBM+3}}^{\text{TMD}} \rangle = 0.446, \text{ and the off-diagonal elements are all close to zero.} \end{aligned}$$

Using these values from projection  $GW$  calculations of the TMD and of the molecule, one can derive from Eq. (B1) that  $\langle \phi_{\text{CBM+2}}^{\text{tot}} | \Sigma | \phi_{\text{CBM+2}}^{\text{tot}} \rangle = 0.654$  eV. This is in very good agreement with the interface  $GW$  calculation

of the CBM+2 of the H<sub>2</sub>Pc:MoS<sub>2</sub> system (the resonance of H<sub>2</sub>Pc LUMO), whose self-energy is 0.667 eV.

- <sup>1</sup>T. Ihn, *Semiconductor Nanostructures: Quantum states and electronic transport* (1st ed. Oxford University Press, 2010).
- <sup>2</sup>D. Jariwala, T. J. Marks, and M. C. Hersam, “Mixed-dimensional van der Waals heterostructures,” *Nat. Mater.* **16**, 170–181 (2017).
- <sup>3</sup>S. Amsterdam, T. K. Stanev, Q. Zhou, A. J.-T. Lou, H. Bergeron, P. Darancet, M. C. Hersam, N. P. Stern, and T. J. Marks, “Electronic coupling in metallophthalocyanine-transition metal dichalcogenide mixed-dimensional heterojunctions,” *ACS Nano* **13**, 4183–4190 (2019).
- <sup>4</sup>Y. L. Huang, Y. J. Zheng, Z. Song, D. Chi, A. T. S. Wee, and S. Y. Quek, “The organic-2D transition metal dichalcogenide heterointerface,” *Chem. Soc. Rev.* **47**, 3241–3264 (2018).
- <sup>5</sup>H. Wang, C. Li, P. Fang, Z. Zhang, and J. Z. Zhang, “Synthesis, properties, and optoelectronic applications of two-dimensional MoS<sub>2</sub> and MoS<sub>2</sub>-based heterostructures,” *Chem. Soc. Rev.* **47**, 6101–6127 (2018).
- <sup>6</sup>J. Sun, Y. Choi, Y. J. Choi, S. Kim, J.-H. Park, S. Lee, and J. H. Cho, “2D-organic hybrid heterostructures for optoelectronic applications,” *Adv. Mater.* **31**, 1803831 (2019).
- <sup>7</sup>J. Choi, H. Zhang, and J. H. Choi, “Modulating optoelectronic properties of two-dimensional transition metal dichalcogenide semiconductors by photoinduced charge transfer,” *ACS Nano* **10**, 1671–1680 (2016).
- <sup>8</sup>D. Jariwala, S. L. Howell, K.-S. Chen, J. Kang, V. K. Sangwan, S. A. Filippone, R. Turrisi, T. J. Marks, L. J. Lauhon, and M. C. Hersam, “Hybrid, gate-tunable, van der waals p-n heterojunctions from pentacene and MoS<sub>2</sub>,” *Nano Lett.* **16**, 497–503 (2016).
- <sup>9</sup>J. Yu, S. Seo, Y. Luo, Y. Sun, S. Oh, C. T. K. Nguyen, C. Seo, J.-H. Kim, J. Kim, and H. Lee, “Efficient and stable solar hydrogen generation of hydrophilic rhodium-disulfide-based photocatalysts via chemically controlled charge transfer paths,” *ACS Nano* **14**, 1715–1726 (2020).
- <sup>10</sup>X. Ling, W. Fang, Y.-H. Lee, P. T. Araujo, X. Zhang, J. F. Rodriguez-Nieva, Y. Lin, J. Zhang, J. Kong, and M. S. Dresselhaus, “Raman enhancement effect on two-dimensional layered materials: Graphene, h-BN and MoS<sub>2</sub>,” *Nano Lett.* **14**, 3033–3040 (2014).
- <sup>11</sup>T. G. Gopakumar, M. Lackinger, M. Hackert, F. Müller, and M. Hietzschold, “Adsorption of palladium phthalocyanine on graphite: STM and LEED Study,” *J. Phys. Chem. B* **108**, 7839–7843 (2004).
- <sup>12</sup>J. Mack and N. Kobayashi, “Low symmetry phthalocyanines and their analogues,” *Chem. Rev.* **111**, 281–321 (2011).
- <sup>13</sup>J. M. Gottfried, “Surface chemistry of porphyrins and phthalocyanines,” *Surf. Sci. Rep.* **70**, 259–379 (2015).
- <sup>14</sup>O. I. Arillo-Flores, M. M. Fadlallah, C. Schuster, U. Eckern, and A. H. Romero, “Magnetic, electronic, and vibrational properties of metal and fluorinated metal phthalocyanines,” *Phys. Rev. B* **87**, 165115 (2013).
- <sup>15</sup>Z.-F. Liu, S. Wei, H. Yoon, O. Adak, I. Ponce, Y. Jiang, W.-D. Jang, L. M. Campos, L. Venkataraman, and J. B. Neaton, “Control of single-molecule junction conductance of porphyrins via a transition-metal center,” *Nano Lett.* **14**, 5365–5370 (2014).
- <sup>16</sup>Q. Zhou, Z.-F. Liu, T. J. Marks, and P. Darancet, “Electronic structure of metallophthalocyanines, MPc (M = Fe, Co, Ni, Cu, Zn, Mg) and fluorinated MPc,” *J. Phys. Chem. A* **125**, 4055–4061 (2021).
- <sup>17</sup>P. Choudhury, L. Ravavarapu, R. Dekle, and S. Chowdhury, “Modulating electronic and optical properties of monolayer MoS<sub>2</sub> using nonbonded phthalocyanine molecules,” *J. Phys. Chem. C* **121**, 2959–2967 (2017).
- <sup>18</sup>T. R. Kafle, B. Kattel, P. Yao, P. Zereshki, H. Zhao, and W.-L. Chan, “Effect of the interfacial energy landscape on photoinduced charge generation at the ZnPc/MoS<sub>2</sub> interface,” *J. Am. Chem. Soc.* **141**, 11328–11336 (2019).
- <sup>19</sup>S. Padgaonkar, S. H. Amsterdam, H. Bergeron, K. Su, T. J. Marks, M. C. Hersam, and E. A. Weiss, “Molecular-orientation-dependent interfacial charge transfer in phthalocyanine/MoS<sub>2</sub> mixed-dimensional heterojunctions,” *J. Phys. Chem. C* **123**, 13337–13343 (2019).
- <sup>20</sup>H. Ahn, Y.-C. Huang, C.-W. Lin, Y.-L. Chiu, E.-C. Lin, Y.-Y. Lai, and Y.-H. Lee, “Efficient defect healing of transition metal dichalcogenides by metallophthalocyanine,” *ACS Appl. Mater. Interfaces* **10**, 29145–29152 (2018).
- <sup>21</sup>L. Hedin, “New method for calculating the one-particle Green’s function with application to the electron-gas problem,” *Phys. Rev.* **139**, A796–A823 (1965).
- <sup>22</sup>G. Strinati, H. J. Mattausch, and W. Hanke, “Dynamical aspects of correlation corrections in a covalent crystal,” *Phys. Rev. B* **25**, 2867–2888 (1982).
- <sup>23</sup>M. S. Hybertsen and S. G. Louie, “Electron correlation in semiconductors and insulators: Band gaps and quasiparticle energies,” *Phys. Rev. B* **34**, 5390–5413 (1986).
- <sup>24</sup>B. D. Malone and M. L. Cohen, “Quasiparticle semiconductor band structures including spin-orbit interactions,” *J. Phys: Condens. Matter* **25**, 105503 (2013).
- <sup>25</sup>N. Kharche, J. T. Muckerman, and M. S. Hybertsen, “First-principles approach to calculating energy level alignment at aqueous semiconductor interfaces,” *Phys. Rev. Lett.* **113**, 176802 (2014).
- <sup>26</sup>M. J. van Setten, F. Caruso, S. Sharifzadeh, X. Ren, M. Scheffler, F. Liu, J. Lischner, L. Lin, J. R. Deslippe, S. G. Louie, C. Yang, F. Weigend, J. B. Neaton, F. Evers, and P. Rinke, “GW100: Benchmarking  $G_0W_0$  for molecular systems,” *J. Chem. Theory Comput.* **11**, 5665–5687 (2015).
- <sup>27</sup>J. P. Perdew, R. G. Parr, M. Levy, and J. L. Balduz, “Density-functional theory for fractional particle number: Derivative discontinuities of the energy,” *Phys. Rev. Lett.* **49**, 1691–1694 (1982).
- <sup>28</sup>W. Yang, A. J. Cohen, and P. Mori-Sánchez, “Derivative discontinuity, bandgap and lowest unoccupied molecular orbital in density functional theory,” *J. Chem. Phys.* **136**, 204111 (2012).
- <sup>29</sup>Y. Yin, P. Miao, Y. Zhang, J. Han, X. Zhang, Y. Gong, L. Gu, C. Xu, T. Yao, P. Xu, Y. Wang, B. Song, and S. Jin, “Significantly increased raman enhancement on MoX<sub>2</sub> (X = S, Se) monolayers upon phase transition,” *Adv. Funct. Mater.* **27**, 1606694 (2017).
- <sup>30</sup>X.-Y. Liu, X.-Y. Xie, W.-H. Fang, and G. Cui, “Theoretical insights into interfacial electron transfer between zinc phthalocyanine and molybdenum disulfide,” *J. Phys. Chem. A* **122**, 9587–9596 (2018).
- <sup>31</sup>S. Haldar, S. Bhandary, H. Vovusha, and B. Sanyal, “Comparative study of electronic and magnetic properties of iron and cobalt phthalocyanine molecules physisorbed on two-dimensional MoS<sub>2</sub> and graphene,” *Phys. Rev. B* **98**, 085440 (2018).
- <sup>32</sup>J. B. Neaton, M. S. Hybertsen, and S. G. Louie, “Renormalization of molecular electronic levels at metal-molecule interfaces,” *Phys. Rev. Lett.* **97**, 216405 (2006).
- <sup>33</sup>K. S. Thygesen and A. Rubio, “Renormalization of molecular quasiparticle levels at metal-molecule interfaces: Trends across binding regimes,” *Phys. Rev. Lett.* **102**, 046802 (2009).
- <sup>34</sup>Z.-F. Liu, F. H. da Jornada, S. G. Louie, and J. B. Neaton, “Accelerating GW-based energy level alignment calculations for molecule-metal interfaces using a substrate screening approach,” *J. Chem. Theory Comput.* **15**, 4218–4227 (2019).
- <sup>35</sup>M. M. Ugeda, A. J. Bradley, S.-F. Shi, F. H. da Jornada, Y. Zhang, D. Y. Qiu, W. Ruan, S.-K. Mo, Z. Hussain, Z.-X. Shen, F. Wang, S. G. Louie, and M. F. Crommie, “Giant bandgap renormalization and excitonic effects in a monolayer transition metal dichalcogenide semiconductor,” *Nat. Mater.* **13**, 1091–1095 (2014).
- <sup>36</sup>F. Xuan, Y. Chen, and S. Y. Quek, “Quasiparticle levels at large interface systems from many-body perturbation theory: The XAF-GW method,” *J. Chem. Theory Comput.* **15**, 3824–3835 (2019).

<sup>37</sup>O. Adeniran, S. Refaelly-Abramson, and Z.-F. Liu, "Layer-dependent quasiparticle electronic structure of the P3HT:PCBM interface from a first-principles substrate screening GW approach," *J. Phys. Chem. C* **124**, 13592–13601 (2020).

<sup>38</sup>L. Shunak, O. Adeniran, G. Voscoboynik, Z.-F. Liu, and S. Refaelly-Abramson, "Exciton modulation in perylene-based molecular crystals upon formation of a metal-organic interface from many-body perturbation theory," *Front. Chem.* **9**, 743391 (2021).

<sup>39</sup>J. Pak, J. Jang, K. Cho, T.-Y. Kim, J.-K. Kim, Y. Song, W.-K. Hong, M. Min, H. Lee, and T. Lee, "Enhancement of photodetection characteristics of MoS<sub>2</sub> field effect transistors using surface treatment with copper phthalocyanine," *Nanoscale* **7**, 18780–18788 (2015).

<sup>40</sup>G. Ghimire, S. Adhikari, S. G. Jo, H. Kim, J. Jiang, J. Joo, and J. Kim, "Local enhancement of exciton emission of monolayer MoS<sub>2</sub> by copper phthalocyanine nanoparticles," *J. Phys. Chem. C* **122**, 6794–6800 (2018).

<sup>41</sup>N. Mutz, S. Park, T. Schultz, S. Sadofev, S. Dalglish, L. Reissig, N. Koch, E. J. W. List-Kratochvil, and S. Blumstengel, "Excited-state charge transfer enabling MoS<sub>2</sub>/phthalocyanine photodetectors with extended spectral sensitivity," *J. Phys. Chem. C* **124**, 2837–2843 (2020).

<sup>42</sup>Y. J. Zheng, Y. L. Huang, Y. Chen, W. Zhao, G. Eda, C. D. Spataru, W. Zhang, Y.-H. Chang, L.-J. Li, D. Chi, S. Y. Quek, and A. T. S. Wee, "Heterointerface screening effects between organic monolayers and monolayer transition metal dichalcogenides," *ACS Nano* **10**, 2476–2484 (2016).

<sup>43</sup>N. Zibouche, M. Schlipf, and F. Giustino, "GW band structure of monolayer MoS<sub>2</sub> using the SternheimerGW method and effect of dielectric environment," *Phys. Rev. B* **103**, 125401 (2021).

<sup>44</sup>J. Ryoo, Y.-S. Kim, K. C. Santosh, and K. Cho, "Monolayer MoS<sub>2</sub> bandgap modulation by dielectric environments and tunable bandgap transistors," *Sci. Rep.* **6**, 29184 (2016).

<sup>45</sup>D. Y. Qiu, F. H. da Jornada, and S. G. Louie, "Environmental screening effects in 2D materials: Renormalization of the bandgap, electronic structure, and optical spectra of few-layer black phosphorus," *Nano Lett.* **17**, 4706–4712 (2017).

<sup>46</sup>Z.-F. Liu, "Dielectric embedding GW for weakly coupled molecule-metal interfaces," *J. Chem. Phys.* **152**, 054103 (2020).

<sup>47</sup>K. Berland and P. Hyldgaard, "Exchange functional that tests the robustness of the plasmon description of the van der Waals density functional," *Phys. Rev. B* **89**, 035412 (2014).

<sup>48</sup>M. Schlipf and F. Gygi, "Optimization algorithm for the generation of ONCV pseudopotentials," *Comput. Phys. Commun.* **196**, 36–44 (2015).

<sup>49</sup>D. R. Hamann, "Optimized norm-conserving Vanderbilt pseudopotentials," *Phys. Rev. B* **88**, 085117 (2013).

<sup>50</sup>P. Giannozzi, S. Baroni, N. Bonini, M. Calandra, R. Car, C. Cavazzoni, D. Ceresoli, G. L. Chiarotti, M. Cococcioni, I. Dabo, A. Dal Corso, S. de Gironcoli, S. Fabris, G. Fratesi, R. Gebauer, U. Gerstmann, C. Gougaudis, A. Kokalj, M. Lazzari, L. Martin-Samos, N. Marzari, F. Mauri, R. Mazzarello, S. Paolini, A. Pasquarello, L. Paulatto, C. Sbraccia, S. Scandolo, G. Sclauzero, A. P. Seitsonen, A. Smogunov, P. Umari, and R. M. Wentzcovitch, "QUANTUM ESPRESSO: A modular and open-source software project for quantum simulations of materials," *J. Phys.: Condens. Matter* **21**, 395502 (2009).

<sup>51</sup>N. Wakabayashi, H. G. Smith, and R. M. Nicklow, "Lattice dynamics of hexagonal MoS<sub>2</sub> studied by neutron scattering," *Phys. Rev. B* **12**, 659–663 (1975).

<sup>52</sup>P. B. James and M. T. Lavik, "The crystal structure of MoSe<sub>2</sub>," *Acta Cryst.* **16**, 1183–1183 (1963).

<sup>53</sup>W. J. Schutte, J. L. De Boer, and F. Jellinek, "Crystal structures of tungsten disulfide and diselenide," *J. Solid State Chem.* **70**, 207–209 (1987).

<sup>54</sup>K. Ulman and S. Y. Quek, "Organic-2D material heterostructures: A promising platform for exciton condensation and multiplication," *Nano Lett.* **21**, 8888–8894 (2021).

<sup>55</sup>K. Momma and F. Izumi, "VESTA: a three-dimensional visualization system for electronic and structural analysis," *J. Appl. Cryst.* **41**, 653–658 (2008).

<sup>56</sup>J. P. Perdew, K. Burke, and M. Ernzerhof, "Generalized gradient approximation made simple," *Phys. Rev. Lett.* **77**, 3865–3868 (1996).

<sup>57</sup>S. Ismail-Beigi, "Truncation of periodic image interactions for confined systems," *Phys. Rev. B* **73**, 233103 (2006).

<sup>58</sup>J. Deslippe, G. Samsonidze, M. Jain, M. L. Cohen, and S. G. Louie, "Coulomb-hole summations and energies for GW calculations with limited number of empty orbitals: A modified static remainder approach," *Phys. Rev. B* **87**, 165124 (2013).

<sup>59</sup>J. Deslippe, G. Samsonidze, D. A. Strubbe, M. Jain, M. L. Cohen, and S. G. Louie, "BerkeleyGW: A massively parallel computer package for the calculation of the quasiparticle and optical properties of materials and nanostructures," *Comput. Phys. Commun.* **183**, 1269–1289 (2012).

<sup>60</sup>A. Ramasubramaniam, "Large excitonic effects in monolayers of molybdenum and tungsten dichalcogenides," *Phys. Rev. B* **86**, 115409 (2012).

<sup>61</sup>I. Tamblyn, P. Darancet, S. Y. Quek, S. A. Bonev, and J. B. Neaton, "Electronic energy level alignment at metal-molecule interfaces with a GW approach," *Phys. Rev. B* **84**, 201402 (2011).

<sup>62</sup>Y. Chen, I. Tamblyn, and S. Y. Quek, "Energy level alignment at hybridized organic–metal interfaces: The role of many-electron effects," *J. Phys. Chem. C* **121**, 13125–13134 (2017).

<sup>63</sup>H. Shi, H. Pan, Y.-W. Zhang, and B. I. Yakobson, "Quasiparticle band structures and optical properties of strained monolayer MoS<sub>2</sub> and WS<sub>2</sub>," *Phys. Rev. B* **87**, 155304 (2013).

<sup>64</sup>F. H. da Jornada, D. Y. Qiu, and S. G. Louie, "Nonuniform sampling schemes of the Brillouin zone for many-electron perturbation-theory calculations in reduced dimensionality," *Phys. Rev. B* **95**, 035109 (2017).

<sup>65</sup>Q. Zhou, Z.-F. Liu, T. J. Marks, and P. Darancet, "Range-separated hybrid functionals for mixed-dimensional heterojunctions: Application to phthalocyanines/MoS<sub>2</sub>," *APL Mater.* in press, arXiv:2107.08516 (2021).

<sup>66</sup>X. Blase, C. Attaccalite, and V. Olevano, "First-principles GW calculations for fullerenes, porphyrins, phthalocyanine, and other molecules of interest for organic photovoltaic applications," *Phys. Rev. B* **83**, 115103 (2011).

<sup>67</sup>H. Zhang, J. Ji, A. A. Gonzalez, and J. H. Choi, "Tailoring photoelectrochemical properties of semiconducting transition metal dichalcogenide nanolayers with porphyrin functionalization," *J. Mater. Chem. C* **5**, 11233–11238 (2017).

<sup>68</sup>E. P. Nguyen, B. J. Carey, C. J. Harrison, P. Atkin, K. J. Berean, E. Della Gaspera, J. Z. Ou, R. B. Kaner, K. Kalantar-zadeh, and T. Daeneke, "Excitation dependent bidirectional electron transfer in phthalocyanine-functionalised MoS<sub>2</sub> nanosheets," *Nanoscale* **8**, 16276–16283 (2016).

<sup>69</sup>A. Raja, A. Chaves, J. Yu, G. Arefe, H. M. Hill, A. F. Rigosi, T. C. Berkelbach, P. Nagler, C. Schüller, T. Korn, C. Nuckolls, J. Hone, L. E. Brus, T. F. Heinz, D. R. Reichman, and A. Chernikov, "Coulomb engineering of the bandgap and excitons in two-dimensional materials," *Nat. Commun.* **8**, 15251 (2017).

<sup>70</sup>F. Tran and P. Blaha, "Importance of the kinetic energy density for band gap calculations in solids with density functional theory," *J. Phys. Chem. A* **121**, 3318–3325 (2017).

<sup>71</sup>H.-J. Sung, D.-H. Choe, and K. J. Chang, "The effects of surface polarity and dangling bonds on the electronic properties of monolayer and bilayer MoS<sub>2</sub> on  $\alpha$ -quartz," *New J. Phys.* **16**, 113055 (2014).

<sup>72</sup>V. V. Afanas'ev, D. Chiappe, M. Perucchini, M. Houssa, C. Huyghebaert, I. Radu, and A. Stesmans, "Impact of MoS<sub>2</sub> layer transfer on electrostatics of MoS<sub>2</sub>/SiO<sub>2</sub> interface," *Nanotechnology* **30**, 055702 (2019).

<sup>73</sup>W. Chen and A. Pasquarello, "Correspondence of defect energy levels in hybrid density functional theory and many-body perturbation theory," *Phys. Rev. B* **88**, 115104 (2013).